The Astrophysical Journal, 814:54 (14pp), 2015 November 20 doi:10.1088/0004-637X/814/1/54

SOFIA/FORCAST OBSERVATIONS OF WARM DUST IN S106: A FRAGMENTED ENVIRONMENT

J. D. Adams[1,2], T. L. Herter[2], J. L. Hora[3], N. Schneider[4], R. M. Lau[2], J. G. Staguhn[5,6], R. Simon[4], N. Smith[7], R. D. Gehrz[8], L. E. Allen[9], S. Bontemps[10], S. J. Carey[11], G. G. Fazio[3], R. A. Gutermuth[12], A. Guzman Fernandez[3], M. Hankins[2], T. Hill[13], E. Keto[3], X. P. Koenig[14], K. E. Kraemer[15], S. T. Megeath[16], D. R. Mizuno[15], F. Motte[17], P. C. Myers[3], and H. A. Smith[3]

[1] Stratospheric Observatory for Infrared Astronomy, Universities Space Research Association, NASA/Armstrong Flight Research Center, 2825 East Avenue P, Palmdale, CA 93550, USA
[2] Department of Astronomy, Cornell University, Space Sciences Building, Ithaca, NY 14853, USA
[3] Harvard-Smithsonian Center for Astrophysics, 60 Garden Street, Cambridge, MA 02138, USA
[4] KOSMA, I. Physikalisches Institut, Universität zu Köln, Zülpicher Strasse 77, D-50937 Köln, Germany
[5] NASA/Goddard Space Flight Center, 8800 Greenbelt Road, Greenbelt, MD 20771, USA
[6] Department of Physics and Astronomy, Johns Hopkins University, 3400 N. Charles Street, Baltimore, MD 21218, USA
[7] Department of Astronomy, University of Arizona, 933 North Cherry Avenue, Tucson, AZ 85721-0065, USA
[8] Minnesota Institute for Astrophysics, University of Minnesota, 116 Church Street SE, Minneapolis, MN 55455, USA
[9] National Optical Astronomy Observatory, 950 North Cherry Avenue, Tucson, AZ 85719, USA
[10] Université Bordeaux, LAB, UMR 5804, CNRS, F-33270, Floirac, France
[11] Spitzer Science Center, California Institute of Technology, 1200 East California Boulevard, Pasadena, CA 91125, USA
[12] Department of Astronomy, University of Massachusetts, LGRT-B 619E, 710 North Pleasant Street, Amherst, MA 01003-9305, USA
[13] Joint ALMA Observatory, 3107 Alonso de Cordova, Vitacura, Santiago, Chile
[14] Department of Astronomy, Yale University, New Haven, CT 06511, USA
[15] Institute for Scientific Research, Boston College, Chestnut Hill, MA 02467, USA
[16] Department of Physics and Astronomy, University of Toledo, 2801 West Bancroft Street, Toledo, OH 43606, USA
[17] Laboratoire AIM Paris Saclay, CEA/Irfu—Université Paris Diderot—CNRS, Centre d'Études de Saclay, F-91191 Gif-sur-Yvette, France
Received 2015 April 28; accepted 2015 October 14; published 2015 November 17

ABSTRACT

We present mid-IR (19–37 μm) imaging observations of S106 from SOFIA/FORCAST, complemented with IR observations from *Spitzer*/IRAC (3.6–8.0 μm), IRTF/MIRLIN (11.3 and 12.5 μm), and *Herschel*/PACS (70 and 160 μm). We use these observations, observations in the literature, and radiation transfer modeling to study the heating and composition of the warm ($\sim$100 K) dust in the region. The dust is heated radiatively by the source S106 IR, with little contributions from grain–electron collisions and Lyα radiation. The dust luminosity is $\gtrsim(9.02 \pm 1.01) \times 10^4\ L_\odot$, consistent with heating by a mid- to late-type O star. We find a temperature gradient ($\sim$75–107 K) in the lobes, which is consistent with a dusty equatorial geometry around S106 IR. Furthermore, the SOFIA observations resolve several cool ($\sim$65–70 K) lanes and pockets of warmer ($\sim$75–90 K) dust in the ionization shadow, indicating that the environment is fragmented. We model the dust mass as a composition of amorphous silicates, amorphous carbon, big grains, very small grains, and polycyclic aromatic hydrocarbons. We present the relative abundances of each grain component for several locations in S106.

Key words: circumstellar matter – H II regions – infrared: stars – radiative transfer – stars: formation

1. INTRODUCTION

Dust plays a critical role in the life cycle of stars and the interstellar medium. Stars form from the gravitational collapse of gas and dust in the interstellar medium, while dust that forms in the ejecta of evolved stars and supernovae enriches the interstellar medium. Dust from evolved stars and supernovae is later available as star-forming material. In star formation regions, the dust both shields the cold inner regions of dense clouds, leading to the conditions necessary for collapse, and can be subsequently heated and processed by stars as they form. Since this dust is a building block for protostellar envelopes and extrasolar planetary systems, the composition and processing of the dust by stellar radiation is worthy of study.

S106 (Sharpless 1959) is a well-studied, large ($\sim$3′), bipolar H II region (Israel & Felli 1978; Lucas et al. 1978; Pipher et al. 1978; Tokunaga & Thompson 1979; Herter et al. 1982) excited by a luminous source (Allen & Penston 1975; Sibille et al. 1975; Gehrz et al. 1982), referred to as S106 IR. Recent analysis performed by Schneider et al. (2007) suggests that S106 is part of the Cygnus-X complex and is located at a distance of $\sim$1.4 kpc, a distance that is substantially farther than some earlier distance estimates of $\sim$600 pc (Eiroa et al. 1979; Staude et al. 1982) and placing it closer to certain OB associations that can affect its surrounding molecular cloud with radiation and winds. S106 presents an opportuntity for us to study the composition and heating of dust in the vicinity of a massive, luminous star.

The effective temperature (37,000–40,000 K) of S106 IR has been determined by analysis of the observed emission line intensities in the ionized region (van den Ancker et al. 2000). This temperature corresponds to a spectral type of O6–O9, depending on the method of calibration applied to model stellar atmospheres that are used for reference (Schaerer et al. 1996; Stasińska & Schaerer 1997; Martins et al. 2005).

Previous work also includes the characterization of the molecular cloud and heating of the gas (Schneider et al. 2002, 2003), as well as the polycyclic aromatic hydrocarbon (PAH) and warm ($\sim$130 K) dust components (Gehrz et al. 1982; Smith et al. 2001) throughout the bipolar nebula. The dust in the bipolar region is concentrated in several bright, compact sources, some of which lie along the bipolar limb. The dust is heated radiatively by S106 IR. In the ionzed

region, there is the possibility for further heating from collisions between grains and electrons, as well as Lyα radiation (Smith et al. 2001). However, the relative contribution to the total dust heating by the non-stellar heating sources have yet to be examined.

It has been known for decades that material around S106 IR casts a UV shadow seen in high spatial resolution radio contiuum images (Bally et al. 1983). The UV shadow bisects the bipolar lobes. Near-IR dark lanes (Hodapp & Rayner 1991; Oasa et al. 2006), PAH emission (Smith et al. 2001), and Hα emission (Bally et al. 1998) are all present within this shadow.

Coincident with the dark lanes is emission from a cold dust bar (Mezger et al. 1987) and recently detected warm CO gas (Simon et al. 2012). Interpretations of the earlier observations invoked the existence of a large ($\sim$30″–60″), continuous disk around S106 IR (Bally & Scoville 1982; Bieging 1984; Mezger et al. 1987). However, higher angular resolution observations presented by Barsony et al. (1989) failed to detect a large, continuous disk containing molecular gas and instead revealed molecular gas fragments. A similar result for the cold dust was confirmed by Richer et al. (1993), whose millimeter observations showed that the cold dust was broken up into several sources. Recent observations of molecular gas velocity from Schneider et al. (2002) do not provide evidence for a large smooth or fragmented disk.

Circumstellar material has been detected at very small distances from S106 IR. VLA observations presented by Gibb & Hoare (2007) provide direct evidence for an ionization wind from circumstellar material located very close ($\sim$60 AU) to S106 IR. Emission from this region is elongated in the directions that are perpendicular to the bipolar lobes. However, Simon et al. (2012) showed that there is also a column of warm, dense CO gas which contributes to the extinction of the stellar flux in addition to the possible existence of a small disk. CO $\nu = 2$–0 bandhead emission, observed and modeled by Murakawa et al. (2013), is confined to a ring at 0.3–4 AU from S106 IR, assuming a stellar mass of 20 $M_{\odot}$. These CO $\nu = 2$–0 observations provide compelling evidence for a disk on AU scales.

In this paper, we present new IR observations from state-of-the-art ground-based, airborne, and space-based facilities, with the aim of characterizing the dust heating and composition. We use radiative transfer modeling to explain the dust equilibrium temperatures and identify a plausible mineral composition for the dust grains. Finally, we discuss the implications that our observations and modeling have for the nature of S106 IR, contribution to the dust heating from non-stellar sources, dust composition in the bipolar region, and the H II region.

2. OBSERVATIONS

2.1. Spitzer/IRAC

S106 was observed with *Spitzer*/IRAC (Fazio et al. 2004; Werner et al. 2004) as part of the IRAC Guaranteed Time Observations (GTO) program (PID 6, AOR 3657472) and during the Cygnus-X Legacy Survey (PID 40184, AORs 27108352, 27107328, 27108608; Hora et al. 2009; Kraemer et al. 2010) at wavelengths of 3.6, 4.5, 5.8, and 8.0 μm. The images were obtained using the 12 s high dynamic range mode, which takes one short (0.6 s) and one long (12 s) frame at each pointing in the map. Part of the region was also observed in the GLIMPSE360 Exploration Science program during the *Spitzer* Warm Mission at 3.6 and 4.5 μm using 12 s frames (PID 61072, AOR 42053120; PI B. Whitney). We used the latest version of the Basic Calibrated Data (BCD) available in the archive[18], which was version 18.7.0 except for AOR 42053120 which was version 18.18.0. The BCD were used rather than the "corrected" or cBCD because the pipeline automatic column pulldown correction causes many artifacts in the data near regions of bright extended emission, as is present in S106. The IRAC images were individually processed using the routine imclean[19] which is an IRAF[20]-based script for removing the bright source artifacts ("pulldown," "muxbleed," and "banding"; Hora et al. 2004; Pipher et al. 2004) from the BCD images. Saturated regions and the resulting artifacts in the 12 s frames were masked as well, allowing the unsaturated short frame data to be used in those locations. The artifact-corrected BCDs were mosaicked into larger images using the IRACproc package (Schuster et al. 2006). IRACproc is a PDL script based on the *Spitzer* Science Center's post-BCD processing software MOPEX (Makovoz & Khan 2005) which has been enhanced for better cosmic ray rejection. The final images have plate scales of 0.″863 per pixel, with intensity units in MJy/sr.

2.2. IRTF/MIRLIN

We include observations taken with the MIRLIN camera (Ressler et al. 1994) at the 3 m NASA Infrared Telescope Facility (IRTF) on 2002, June 13. These observations include images taken through the CVF at a wavelength of 11.300 μm and through the N5 filter at a center wavelength of 12.492 μm. The MIRLIN plate scale at the IRTF is 0.″47 per pixel on the 128 × 128 Si:As BIB array. The observations were taken in chop/nod mode with cumulative integration times of 360 s and 112.5 s for 11.300 μm and 12.492 μm, respectively. The chopper throw was 30″ east/west with a similar north/south telescope nod that we varied slightly from one set of images to the next. After sky subtraction, the many individual frames were resampled to a smaller pixel scale (0.″12 per pixel) and then shifted and added using the bright central star for spatial registration. The observations were flux-calibrated using observations of β Peg taken immediately after S106, adopting the zero-magnitude fluxes in the MIRLIN handbook.

2.3. SOFIA/FORCAST

We observed S106 with the FORCAST instrument (Adams et al. 2012a; Herter et al. 2012) on SOFIA (Young et al. 2012) at the wavelengths 19.7, 25.3, 31.5, and 37.1 μm, using FORCAST guaranteed observing time during Cycle 1 (Flight 108 on 2013, June 21) and Cycle 2 (Flight 170 on 2014, May 8). FORCAST is a dual channel imager and spectrometer that utilizes a 256 × 256 pixel format Si:As detector for 5–26 μm and a 256 × 256 pixel format Si:Sb detector for 26–40 μm, with a rectified plate scale of 0.″768 per pixel in each camera. The wavelengths 19.7, 25.3, and 31.5 μm were observed using the dichroic beamsplitter, while 37.1 μm was observed directly. The observations were performed with off-source chopping and nodding (C2NC2 mode) and dithering, whereby the off-source

[18] http://irsa.ipac.caltech.edu/data/SPITZER/docs/spitzerdataarchives/

[19] See http://irsa.ipac.caltech.edu/data/SPITZER/docs/dataanalysistools/tools/contributed/irac/imclean/

[20] IRAF is distributed by the National Optical Astronomical Observatories, operated by the Association of the Universities for Research in Astronomy, Inc., under cooperative agreement with the National Science Foundation.

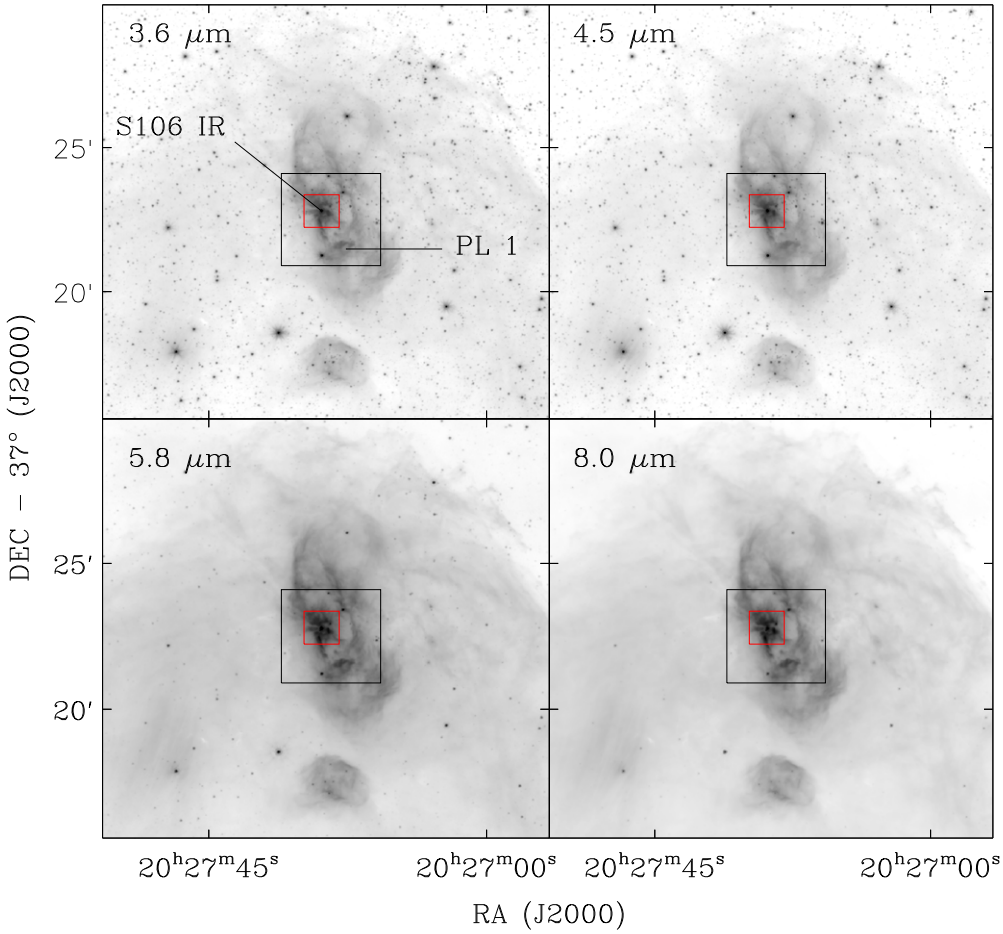

Figure 1. Combined long (12 s) and short (0.6 s) exposure IRAC images of S106 at 3.6, 4.5, 5.8, and 8.0 μm. The displayed image intensities are stretched logarithmically. The locations of S106 IR and the clump PL 1 are indicated in the upper left panel. The black boxed region denotes the size of the FORCAST field of view (without showing the observed SOFIA field rotations), while the red boxed region shows the MIRLIN field of view. These images trace ionization lines, PAH emission, and thermal continuum emission (van den Ancker et al. 2000), as well as young stellar objects and photospheres.

fields were chosen to be ones free of detectable emission in *Midcourse Space Experiment* (Price et al. 2001) 21 μm images. Typical dwell times in each nod beam/dither position were approximately 30–90 s, including chopping inefficiencies.

The raw data were reduced and calibrated using the pipeline described in Herter et al. (2013). This pipeline performs chop and nod subtraction and applies corrections for droop, detector nonlinearity, multiplexer crosstalk, and optical distortion. Calibration factors were derived from the average photometric instrument response to standard stars observed during each corresponding observing campaign (a series of four or more flights). The dither positions were aligned and averaged, producing images with effective on-source exposure times of 480, 371, 375, and 195 s for 19.7, 25.3, 31.5, and 37.1 μm, respectively. The rectified plate scale for all the FORCAST images was $0\farcs768$ per pixel. The effective rms noise levels were approximately 8, 10, 10, and 13 mJy/pixel for 19.7, 25.3, 31.5, and 37.1 μm, respectively. We estimate the calibration error due to flat fielding to be $\sim$10%.

We performed image deconvolution on the FORCAST images using several iterations of a maximum likelihood algorithm (Richardson 1972; Lucy 1974) to produce images with an effective spatial resolution of $\sim 2\farcs4$. The application of this algorithm requires a point-spread function (PSF) to be used as input. We chose to use a synthetic PSF since there were no point sources in the field that were sufficiently bright to use as a reliable reference PSF. The synthetic PSF was a convolution of an Airy function for telescope diffraction and a two-dimensional Gaussian for pointing instability that was scaled so that the FWHMs of the final PSF matched those of the point sources in the images that were to be deconvolved (De Buizer et al. 2012).

Finally, we derived astrometric solutions (WCS) for the images using the location of three point sources in the field and a tangent plane projection. This method produces astrometry that is accurate to within $\sim 0\farcs4$ (Adams et al. 2012b). The astrometrically calibrated frames were then aligned with and sampled to that of the IRAC 3.6 μm image ($0\farcs863$ per pixel), whose astrometric solution is determined from the position of the field stars in the 2MASS catalog.

2.4. Herschel/PACS

In this paper, we use *Herschel*/PACS (Poglitsch et al. 2010) 70 and 160 μm observations from the *Herschel* Open-Time program OT2_jhora_2 (obsIDs 1342257386 and 1342257387). The data were taken on 2012, December 18, simultaneously with SPIRE (Griffin et al. 2010) and PACS, using a scanning speed of $60'' \, s^{-1}$ with one repetition in the nominal and orthogonal observing directions. The individual scan directions of the PACS data were first reduced from the raw data of

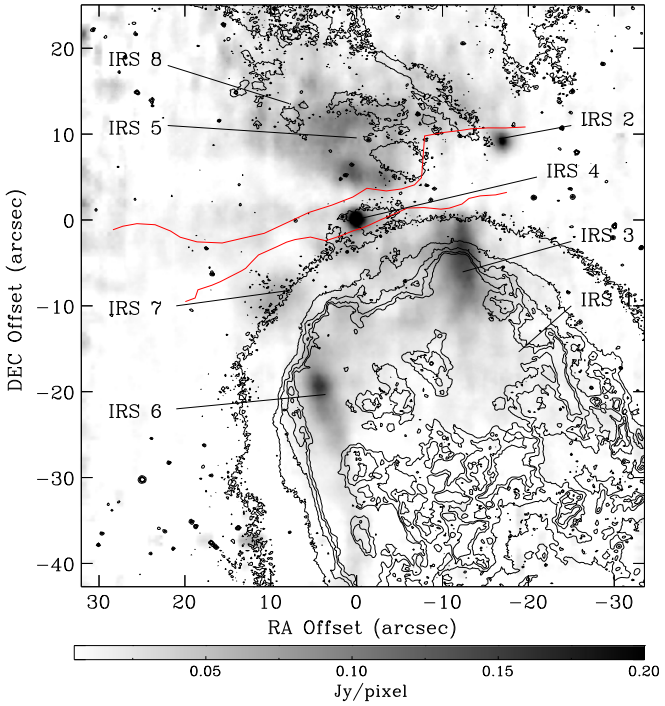

Figure 2. IRTF/MIRLIN image of S106 at 11.3 μm. The image is centered on the coordinates R.A. = $20^{h}27^{m}26\overset{s}{.}74$, decl. = $+37°22'48\overset{''}{.}7$(J2000), near S106 IR. The emission in this images is primarily from PAHs. The locations of the IRS sources from Gehrz et al. (1982) are indicated. The black contours represent Hα emission (Bally et al. 1998). The region between the red lines is devoid of 5 GHz emission (Bally et al. 1983).

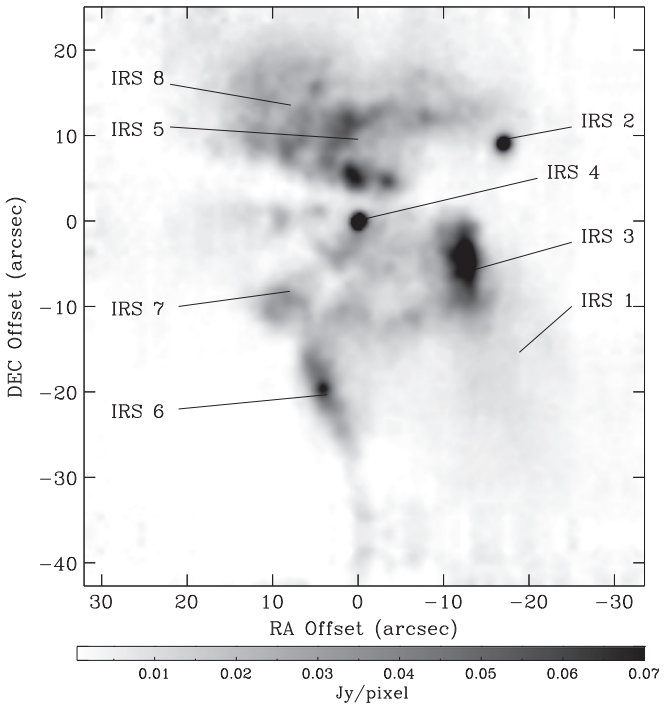

Figure 3. Same as Figure 2, but for 12.492 μm, which traces the dust thermal continuum.

level-0 to level-1 using the standard pipeline in HIPE 10.2751. This includes flat-field and nonlinearity corrections. The next step (from level-1 to level-2) was performed within Scanamorphos v.21 (Roussel 2013). The processing consists of subtracting long and short timescale drifts and masking glitches and brightness discontinuities. The two scan directions were merged and projected onto a spatial grid of 2″/pixel and 3″/pixel for 70 μm and 160 μm, respectively. The angular resolution of the data is 6″ × 12″ for 70 μm and 12″ × 16″ for 160 μm, respectively (PACS Manual v.2.5.1). The absolute calibration uncertainties for the integrated source flux densities are estimated to be ∼10% for 70 μm and ∼20% for 160 μm.

3. OBSERVATIONAL RESULTS

3.1. Morphology

Figure 1 shows the *Spitzer*/IRAC images. Based on the spectrum of S106 presented by van den Ancker et al. (2000), these images trace dust continuum emission, recombination line emission, and PAH emission. In addition, the images contain stars with primarily photospheric emission and young stellar objects that exhibit infrared excess emission. The thermal emission is bipolar. A dark lane is seen in the region where a similar feature is seen in the near-IR (Oasa et al. 2006). There is also emission from a dusty clump (PL 1) to the southwest of the S106 IR as indicated in Figure 1.

The MIRLIN 11.3 μm and 12.492 μm images are shown in Figures 2 and 3, respectively. Although the 11.3 μm image is not continuum subtracted, the emission is dominated by PAHs, while emission at 12.492 μm traces that of the dust thermal continuum. Emission can be seen from the bright, compact sources (IRS 1–8) listed in Gehrz et al. (1982), but also from the lobes. The dark lane seen in near-IR images is also dark at both these wavelengths. In Figure 2, we show the locations of the ionized region using Hα contours (Bally et al. 1998) and the UV shadow as the region devoid of 5 GHz free–free emission (Bally et al. 1983). The position PL 1 lies outside the MIRLIN field.

The deconvolved SOFIA/FORCAST images are shown in Figure 4. Emission was detected from both lobes and from several bright, compact sources. Several of these sources (IRS 1, IRS 3, IRS 5, IRS 6, IRS 7, IRS 8) were detected in ground-based images at ∼10 and ∼18 μm by Gehrz et al. (1982) and Smith et al. (2001) and are indicated in Figure 4. We did not detect the photosphere of S106 IR (IRS 4) at 19–37 μm. The dusty clump PL 1 was detected at all wavelengths by FORCAST.

The *Herschel*/PACS images are shown in Figures 5 and 6. At 70 μm, the morphology follows that of the warm dust continuum that is seen at 19–37 μm. At 160 μm, the morphology changes dramatically due to detection of cold dust in the molecular cloud, and resembles the submillimeter continuum emission (Simon et al. 2012). A cavity is seen surrounding the western region around the lobes, which extends southward along the eastern and western sides of PL 1.

The peak emission at the illuminated edge of PL 1 shifts deeper into the molecular cloud at 160 μm when compared with emission at 37 and 70 μm (Figure 7), suggesting that the clump is self-absorbing. The amount of this shift is nearly 0.05 pc in projection. In addition, the peak of the PAH emission (Smith et al. 2001) lies at the inner edge of the clump and starts to decrease where the 37 μm emission from larger grains peaks.

3.2. Dust Luminosity

In Table 1, we report the total detected dust continuum flux densities at 12–160 μm. We include the flux density at 350 μm

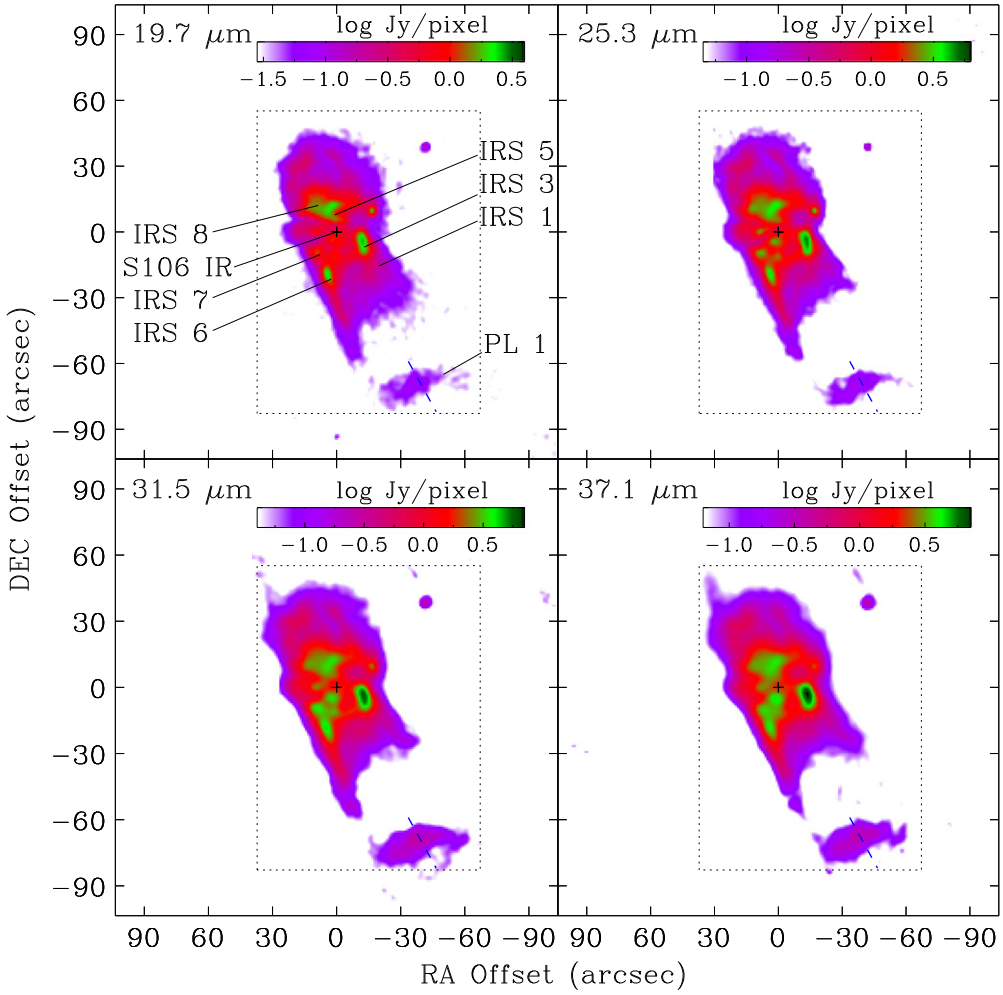

Figure 4. Deconvolved SOFIA/FORCAST images of S106 at 19.7, 25.3, 31.5, and 37.1 μm. The image is centered on the coordinates R.A. = $20^{\rm h}27^{\rm m}26\overset{\rm s}{.}74$, decl. = $+37°22'48\overset{''}{.}7$(J2000), near S106 IR, with the north direction up and east direction to the left. The deconvolved beam size is $2\overset{''}{.}4$. Edge-of-frame artifacts outside the emission regions have been removed for display purposes. Extended sources (IRS 1, 3, 5, 6, 7, 8) detected by Gehrz et al. (1982) at ~10 μm and PL 1 are identified in the upper left panel. The dotted box represents the aperture that was used to compute the total flux (Section 3.2 and Table 1). The blue dashed line indicates the location of the profile shown in Figure 7.

(Simon et al. 2012). The aperture was chosen for each wavelength according to field of view and the extent of the detected dust emission. We limited the aperture at 70 and 160 μm in order to minimize the chance of the inclusion of dust that may be heated by external stars. We examined the 70/160 μm color temperature in this aperture and did not find a gradient that would indicate external heating. The apertures for the FORCAST and *Herschel* images are shown in Figures 4–6. The flux densities of the point sources IRS 2 and IRS 4 have been subtracted (where applicable). From these flux densities, we derive a lower limit to the total dust luminosity of $L_{\rm dust} \gtrsim (9.02 \pm 1.01) \times 10^4\ L_\odot$. We state the luminosity as a lower limit because the some of the stellar radiation may be escaping through the bipolar geometry and there may be dust emission outside the 70 and 160 μm apertures.

3.3. 19/37 μm Color Temperature

A modified blackbody color temperature map derived from the 19 and 37 μm flux ratios is shown in Figure 8 with Hα emission (Bally et al. 1998) overlaid with contours. For this map, the emissivity of the dust grains was assumed to be proportional to $\lambda^{-1.8}$ (Abergel et al. 2011). Overall, the dust temperatures are lower (~70–90 K) in the equatorial region and tend to increase out into the lobes (~107 K).

We resolved several cool lanes in the S106 IR UV shadow, with temperatures of ~70 K, and three compact regions in the UV shadow with temperatures of ~90 K. One of these warmer regions was identified as a 10 μm compact source (IRS 7) by Gehrz et al. (1982).

Figure 8 also depicts the locations used for dust modeling (Section 4). The positions and fluxes at these locations are listed in Table 2.

3.4. 37 μm Optical Depth

Using the temperature map shown in Figure 8 and the 37 μm image, we computed the optical depth τ along the line of sight. We show this optical depth map in Figure 9. The highest column densities ($0.08 \lesssim \tau \lesssim 0.12$) are located near S106 IR, in the UV shadow, with the lobes becoming increasingly optically thin ($\tau \lesssim 0.08$) at larger distances in the lobes. The FORCAST images have low signal-to-noise ratios between IRS 6 and PL 1, indicating a low dust column density or absence of dust in this area.

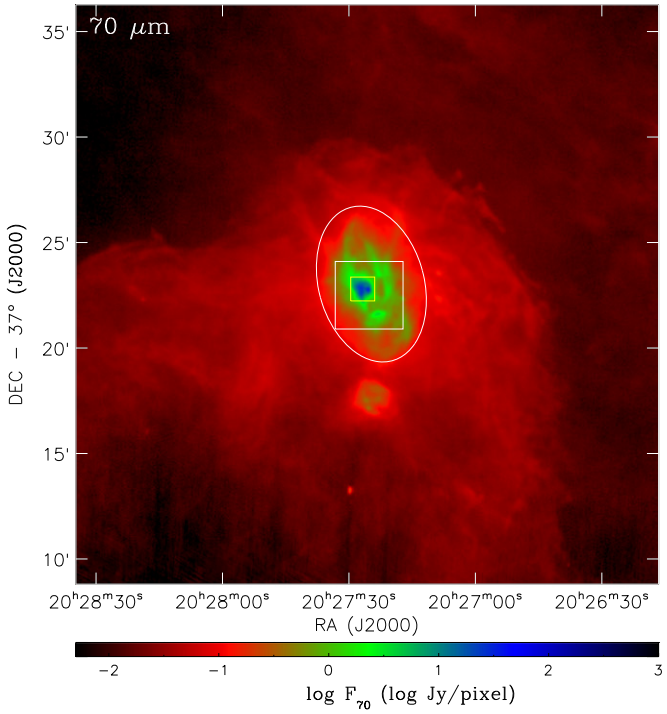

Figure 5. *Herschel*/PACS image of S106 at 70 μm from the Cygnus-X Open-Time program (OT2_jhora_2). The white box represents the FORCAST field of view while the region outlined in yellow represents the MIRLIN field of view. The white ellipse represents the aperture that was used to compute the total flux (Section 3.2 and Table 1).

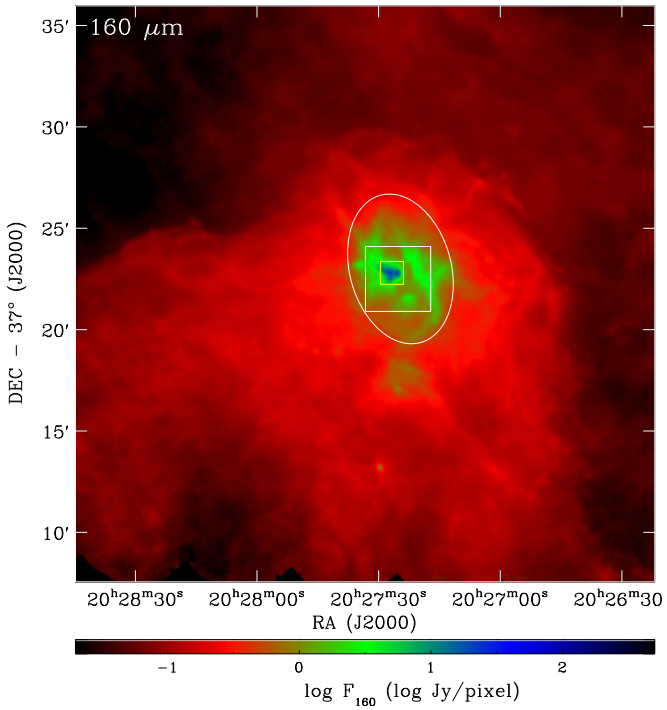

Figure 6. Same as Figure 5, but for 160 μm.

4. DUST MODELING

We used radiation transfer to model the spectral energy distribution (SED) of the dust at the locations specified in Figure 8. Non-stellar components to the dust heating are addressed in Section 5. We used the DustEM software

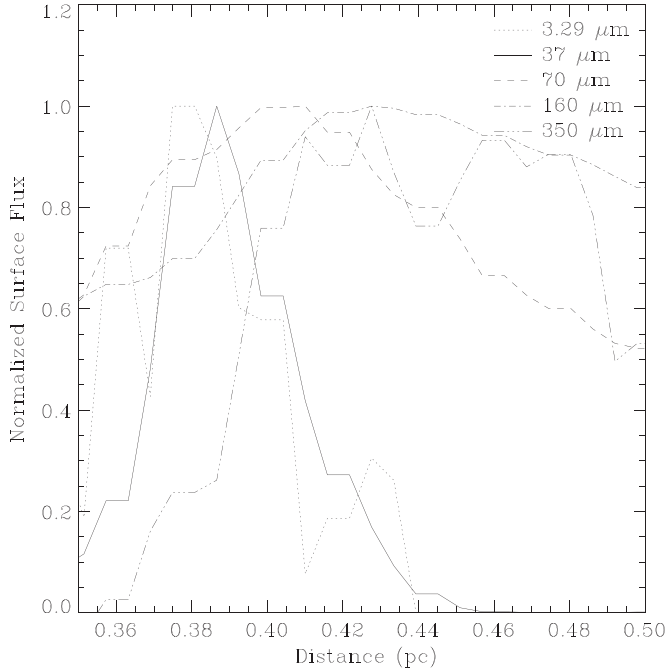

Figure 7. Radial profile (as indicated in Figure 4) through the location PL 1 at 3.29 (Smith et al. 2001), 37, 70, 160, and 350 μm (Simon et al. 2012). The distance from S106 IR is the projected distance, assuming a distance of 1.4 kpc to the region (Schneider et al. 2007). The peak of the PAH emission lies at the inner edge of the clump and is slightly displaced from the peak 37 μm emission, while the peak emission shifts to deeper locations in the clump with increasing wavelength.

Table 1
Total Dust Continuum Flux Densities in S106, Including 350 μm Data from Simon et al. (2012)

λ (μm)	Aperture	F_ν (kJy)
12.492	1.″01 × 1.″11	0.0649 ± 0.0130
19.7	1.″74 × 2.″30	2.53 ± 0.25
25.3	1.″74 × 2.″30	4.32 ± 0.43
31.5	1.″74 × 2.″30	5.66 ± 0.57
37.1	1.″74 × 2.″30	6.86 ± 0.69
70	4.″97 × 7.″53 elliptical	19.1 ± 1.9
160	4.″97 × 7.″53 elliptical	15.8 ± 3.2
350	5.″72 × 4.″05	0.630 ± 0.126

Note. The values exclude emission from the point sources S106 IR and IRS 2 (Gehrz et al. 1982).

(Compiègne et al. 2011) to specify the dust model population and compute its IR emission in a stellar radiation field.

4.1. Radiation Field

At a location within the nebula, the incident radiation field from the star is $(R_*/D)^2 F_{\lambda,*} e^{-\tau_\lambda}$, where R_* is the radius of the star, D is the distance from the stellar surface to the dust, $F_{\lambda,*}$ is the flux density of the star at the surface of the star, and τ_λ is the optical depth of the dust between the star and the location. The distance from the star to the dust was set to the projected distance ($D_{\rm proj}$) between them, scaled to a distance of 1.4 kpc (Schneider et al. 2007). We adopt $\tau_\lambda = \tau_{\rm UV}(121.5\ {\rm nm}/\lambda)^\beta$, where $\beta = 1.85$ (Landini et al. 1984) and $\tau_{\rm UV}$ is a free parameter. For the stellar flux density, we used a stellar atmosphere with a spectral type of O7V and an effective temperature of 37,000 K from Castelli & Kurucz (2004).

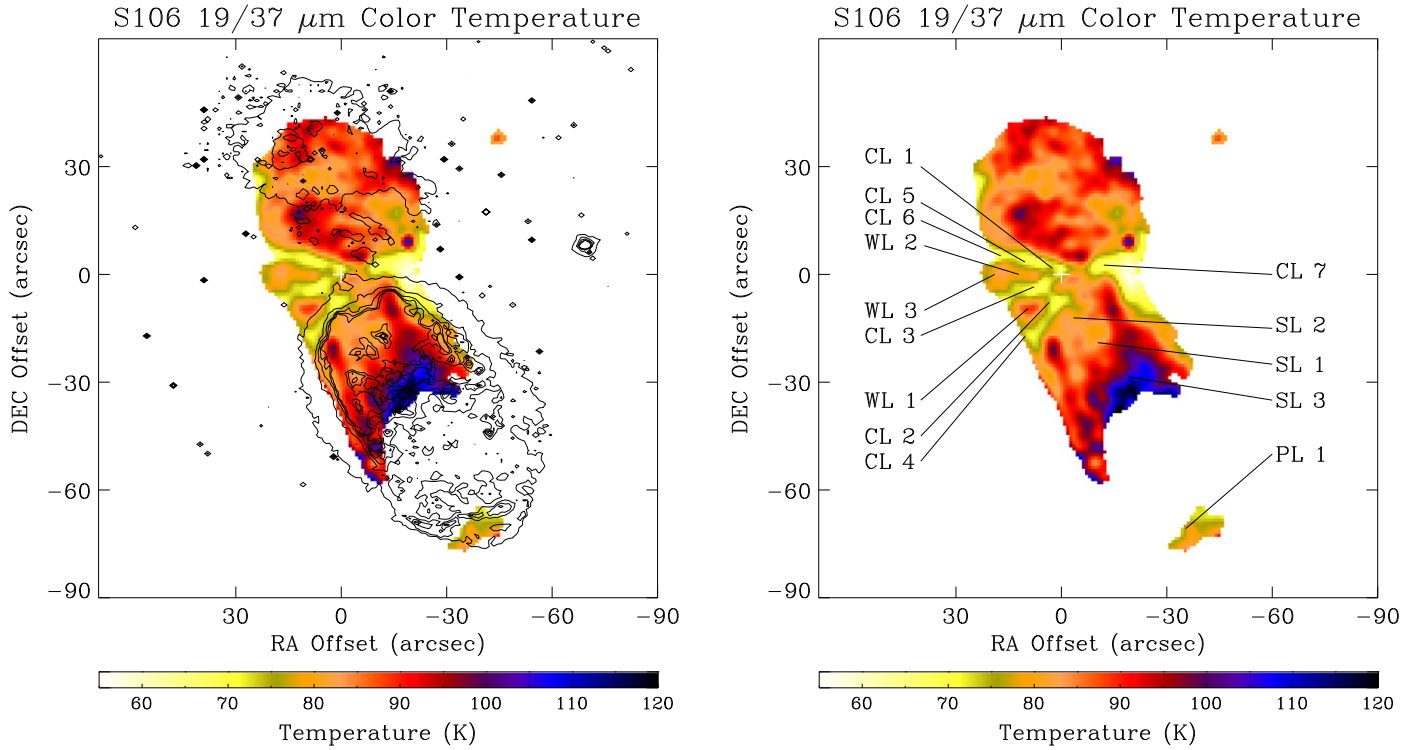

Figure 8. Color–temperature map derived from the FORCAST 19.7 and 37.1 flux maps, assuming a dust emissivity law that is proportional to $\lambda^{-1.8}$ (Abergel et al. 2011). The coordinates of the map are centered near S106 IR and the coordinates are given in the caption to Figure 4. Left: color–temperature map, overlaid with contours of Hα emission (Bally et al. 1998). The UV shadow cone is resolved into cool lanes separated by compact regions of warmer dust. The hottest dust is found in the lobes. Right: the color temperature map with representative dust modeling positions (see Section 4) indicated.

4.2. Grain Types and Size Distributions

For the dust component, we consider contributions to the emission from amorphous silicates (Draine & Li 2007), amorphous carbon, neutral PAHs, and ionized PAHs (Compiègne et al. 2010). In cases of relatively low extinction, we consider emission from both very small ($1.2 \times 10^{-7} \leqslant a \leqslant 1.5 \times 10^{-6}$ cm, where a is the grain radius) grains (VSGs), which can be transiently heated in a UV radiation field (Ryter et al. 1987), and big ($1.5 \times 10^{-6} \leqslant a \leqslant 1.1 \times 10^{-5}$ cm) grains (BGs), which are thought to be composed of silicates (Désert et al. 1990). The grain size distribution for both PAH species is modeled as

$$\frac{dn}{d\,\log a} \propto \frac{e^{-\log\left(\frac{a}{a_0}\right)^2}}{\sigma} \quad (1)$$

where $3.1 \times 10^{-8}\,\mathrm{cm} \leqslant a \leqslant 1.2 \times 10^{-7}\,\mathrm{cm}$, $a_0 = 3.1 \times 10^{-8}\,\mathrm{cm}$, and $\sigma = 0.4$. The grain size distributions for the amorphous silicates, amorphous carbon, VSGs, and BGs were modeled as $dn/da \propto a^{\alpha}$ with α as a free parameter for each species. For the amorphous grains, $3.1 \times 10^{-8}\,\mathrm{cm} \leqslant a \leqslant 2.0 \times 10^{-4}\,\mathrm{cm}$, for VSGs, $1.2 \times 10^{-7}\,\mathrm{cm} \leqslant a \leqslant 1.5 \times 10^{-6}\,\mathrm{cm}$, and for BGs, $1.5 \times 10^{-6}\,\mathrm{cm} \leqslant a \leqslant 1.1 \times 10^{-5}\,\mathrm{cm}$.

4.3. SED Modeling

In Figure 8, we specify locations in the nebula for which we show the SED and perform dust SED modeling. These locations are cool lane positions CL 1–7, warm lane positions WL 1–3, southern lobe positions SL 1–3, southwestern clump position PL 1, and the positions of the bright, compact sources IRS 1, IRS 3, IRS 5, IRS 6, IRS 7, and IRS 8 identified in Gehrz et al. (1982). In Figures 10 and 11, we show the SEDs for these positions, including 3.29 μm IRTF/NSFCAM data from Smith et al. (2001) and 350 μm CSO/SHARC-II data from Simon et al. (2012).

For CL 1–7, the dust composition is assumed to be dominated by a mixture of amorphous silicates, amorphous carbon, and PAHs (Figure 10). Positions CL 1–3 contain contamination from the S106 IR photosphere at 3.29–8.0 μm, and those data are not shown in the SEDs. For CL 1, some PAH emission may be present at 11.3 μm, but these components are not modeled as the ionization fraction is unconstrained. For CL 2, we model the PAH components and note that the ionized PAH component is an upper limit based on emission at 3.29 and 11.3 μm. At CL 3, there is emission at 3.29 μm but not at 11.3 μm. In this case, the PAH components are not modeled as the ionization fraction is unconstrained. For CL 4, we show 3σ upper limits at 3.29 and 12.492 μm. At this position, the IRAC 3.6 and 4.5 μm points help constrain the size distribution for amorphous carbon. Emission at 11.3 μm is used to place an upper limit on the PAH emission, which underpredicts the emission at 5.8 μm. There is a possibility that the IRAC photometry at this position is affected by emission from IRS 6. At CL 5, the 3σ upper limit for 3.29 μm and 4σ upper limit for 12.492 μm are shown. Again, the IRAC fluxes at 3.6 and 4.5 μm help constrain the size distribution for amorphous carbon. For CL 6, a 3σ upper limit at 3.29 μm is shown. At position CL 7, the IRAC data points are contaminated by emission from IRS3 and are shown as upper limits. A 3σ upper limit is shown for 12.492 μm.

The modeling parameters and results for the CL positions are given in Table 3. The modeling results yield values of τ_{UV} in

Table 2
Flux Densities, in Units of log Jy, at the Locations Indicated in Figure 8

Location	R.A. (2000)	decl.	3.29 μm	3.6 μm	4.5 μm	5.8 μm	8.0 μm	11.3 μm
CL 1	20:27:27.03	+37:22:50.5	−1.93 ± −3.00	−1.88 ± −5.12	−1.62 ± −5.28	−1.20 ± −4.51	−1.01 ± −4.09	−1.28 ± −1.97
CL 2	20:27:27.11	+37:22:41.0	−2.04 ± −3.00	−2.20 ± −5.12	−2.14 ± −5.28	−1.57 ± −4.51	−1.20 ± −4.09	−1.05 ± −1.97
CL 3	20:27:27.39	+37:22:45.4	−2.19 ± −3.00	−2.41 ± −5.12	−2.39 ± −5.28	−1.73 ± −4.51	−1.31 ± −4.09	−1.92 ± −1.97
CL 4	20:27:27.69	+37:22:31.6	−2.43 ± −3.00	−2.77 ± −5.12	−2.69 ± −5.28	−1.73 ± −4.51	−1.40 ± −4.09	< −1.97
CL 5	20:27:27.67	+37:22:53.1	−2.90 ± −3.00	−2.70 ± −5.12	−2.53 ± −5.28	−1.90 ± −4.51	−1.47 ± −4.09	−1.33 ± −1.97
CL 6	20:27:28.25	+37:22:54.1	…	−3.09 ± −5.12	−2.92 ± −5.28	−2.01 ± −4.51	−1.58 ± −4.09	−1.66 ± −1.97
CL 7	20:27:25.80	+37:22:51.2	−2.44 ± −3.00	−2.45 ± −5.12	−2.37 ± −5.28	−1.77 ± −4.51	−1.34 ± −4.09	−1.43 ± −1.97
WL 1	20:27:27.61	+37:22:39.4	−1.52 ± −3.00	−2.22 ± −5.60	−2.20 ± −5.76	−1.44 ± −4.99	−1.02 ± −4.57	−0.63 ± −1.97
WL 2	20:27:27.82	+37:22:48.9	−1.93 ± −3.00	−2.48 ± −5.60	−2.37 ± −5.76	−1.67 ± −4.99	−1.27 ± −4.57	−1.08 ± −1.97
WL 3	20:27:28.33	+37:22:48.1	−2.45 ± −3.00	−2.72 ± −5.60	−2.65 ± −5.76	−1.73 ± −4.99	−1.34 ± −4.57	−1.47 ± −1.97
IRS 1	20:27:25.24	+37:22:32.2	−2.39 ± −3.00	−2.74 ± −5.60	−2.69 ± −5.76	−1.99 ± −4.99	−1.54 ± −4.57	−1.09 ± −1.97
IRS 3	20:27:25.66	+37:22:42.6	−1.41 ± −3.00	−1.96 ± −5.60	−1.84 ± −5.76	−1.19 ± −4.99	−0.75 ± −4.57	−0.29 ± −1.97
IRS 5	20:27:26.80	+37:22:57.3	−1.85 ± −3.00	−2.11 ± −5.60	−2.00 ± −5.76	−1.45 ± −4.99	−0.95 ± −4.57	−0.51 ± −1.97
IRS 6	20:27:27.19	+37:22:29.0	−1.42 ± −3.00	−2.00 ± −5.60	−1.96 ± −5.76	−1.24 ± −4.99	−0.80 ± −4.57	−0.27 ± −1.97
IRS 7	20:27:27.40	+37:22:39.3	−1.66 ± −3.00	−2.22 ± −5.60	−2.13 ± −5.76	−1.44 ± −4.99	−1.01 ± −4.57	−0.54 ± −1.97
IRS 8	20:27:27.45	+37:23:00.9	−1.82 ± −3.00	−2.25 ± −5.60	−2.18 ± −5.76	−1.48 ± −4.99	−1.03 ± −4.57	−0.86 ± −1.97
SL 1	20:27:25.96	+37:22:28.8	−2.15 ± −3.00	−2.55 ± −5.60	−2.56 ± −5.76	−1.79 ± −4.99	−1.37 ± −4.57	−1.84 ± −1.97
SL 2	20:27:26.46	+37:22:35.8	−1.83 ± −3.00	−2.21 ± −5.60	−2.17 ± −5.76	−1.55 ± −4.99	−1.12 ± −4.57	−0.82 ± −1.97
SL 3	20:27:25.25	+37:22:21.0	−2.52 ± −3.00	−3.06 ± −5.60	−2.93 ± −5.76	−2.33 ± −4.99	−1.90 ± −4.57	−1.78 ± −1.97
PL 1	20:27:23.84	+37:21:37.8	−2.11 ± −3.00	−2.58 ± −5.60	−2.62 ± −5.76	−1.76 ± −4.99	−1.35 ± −4.57	…

Location	12.492 μm	19.7 μm	25.3 μm	31.5 μm	37.1 μm	70 μm	160 μm	350 μm
CL 1	−1.53 ± −2.67	−0.19 ± −1.18	0.27 ± −0.73	0.44 ± −0.56	0.62 ± −0.38	0.79 ± −0.21	0.30 ± −0.40	−0.61 ± −2.19
CL 2	−1.40 ± −2.67	−0.11 ± −1.11	0.37 ± −0.63	0.62 ± −0.38	0.74 ± −0.26	0.77 ± −0.23	0.24 ± −0.46	−0.86 ± −2.19
CL 3	−1.74 ± −2.67	−0.39 ± −1.38	0.03 ± −0.97	0.33 ± −0.67	0.49 ± −0.51	0.77 ± −0.23	0.31 ± −0.39	−0.70 ± −2.19
CL 4	< −2.67	−0.77 ± −1.73	−0.29 ± −1.28	0.04 ± −0.96	−0.00 ± −1.00	0.60 ± −0.40	0.14 ± −0.55	−0.88 ± −2.19
CL 5	…	−0.36 ± −1.36	0.08 ± −0.91	0.36 ± −0.64	0.46 ± −0.54	0.79 ± −0.21	0.34 ± −0.36	−0.51 ± −2.19
CL 6	−2.01 ± −2.67	−0.63 ± −1.61	−0.11 ± −1.11	0.16 ± −0.84	0.16 ± −0.84	0.62 ± −0.38	0.29 ± −0.41	−0.49 ± −2.19
CL 7	−1.91 ± −2.67	−0.38 ± −1.37	−0.03 ± −1.03	0.33 ± −0.67	0.53 ± −0.47	0.77 ± −0.23	0.31 ± −0.39	−0.38 ± −2.19
WL 1	−0.98 ± −2.67	0.25 ± −0.75	0.59 ± −0.41	0.76 ± −0.24	0.65 ± −0.35	0.72 ± −0.28	0.23 ± −0.47	−0.74 ± −2.19
WL 2	−1.27 ± −2.67	−0.12 ± −1.12	0.27 ± −0.73	0.44 ± −0.56	0.45 ± −0.55	0.72 ± −0.28	0.32 ± −0.38	−0.63 ± −2.19
WL 3	−1.74 ± −2.67	−0.36 ± −1.35	0.03 ± −0.97	0.14 ± −0.86	0.14 ± −0.86	0.50 ± −0.50	0.20 ± −0.49	−0.75 ± −2.19
IRS 1	−1.35 ± −2.67	−0.42 ± −1.42	−0.29 ± −1.29	−0.21 ± −1.21	−0.12 ± −1.12	−0.01 ± −1.01	−0.36 ± −1.06	< −2.19
IRS 3	−0.57 ± −2.67	0.58 ± −0.42	0.82 ± −0.18	0.91 ± −0.09	0.90 ± −0.10	0.72 ± −0.28	0.24 ± −0.46	−1.02 ± −2.19
IRS 5	−0.85 ± −2.67	0.36 ± −0.64	0.59 ± −0.41	0.64 ± −0.36	0.74 ± −0.26	0.63 ± −0.37	0.15 ± −0.55	−0.77 ± −2.19
IRS 6	−0.69 ± −2.67	0.44 ± −0.56	0.68 ± −0.32	0.71 ± −0.29	0.71 ± −0.29	0.47 ± −0.53	−0.05 ± −0.75	−1.38 ± −2.19
IRS 7	−0.84 ± −2.67	0.23 ± −0.77	0.65 ± −0.35	0.78 ± −0.22	0.76 ± −0.24	0.75 ± −0.25	0.24 ± −0.46	−0.78 ± −2.19
IRS 8	−0.93 ± −2.67	0.41 ± −0.59	0.63 ± −0.37	0.66 ± −0.34	0.71 ± −0.29	0.62 ± −0.38	0.09 ± −0.61	−0.89 ± −2.19
SL 1	−1.65 ± −2.67	−0.47 ± −1.47	−0.25 ± −1.25	−0.08 ± −1.08	−0.05 ± −1.05	0.12 ± −0.88	−0.29 ± −0.99	−1.94 ± −2.19
SL 2	−1.15 ± −2.67	0.03 ± −0.97	0.34 ± −0.66	0.50 ± −0.50	0.55 ± −0.45	0.49 ± −0.51	0.01 ± −0.69	−1.18 ± −2.19
SL 3	−1.61 ± −2.67	−0.72 ± −1.71	−0.67 ± −1.65	−0.80 ± −1.77	−0.67 ± −1.64	−0.41 ± −1.41	−0.69 ± −1.39	…
PL 1	…	−0.86 ± −1.84	−0.57 ± −1.56	−0.34 ± −1.34	−0.28 ± −1.28	−0.12 ± −1.12	−0.59 ± −1.29	−2.08 ± −2.19

Note. The table includes flux densities at 3.29 μm (Smith et al. 2001) and 350 μm (Simon et al. 2012).

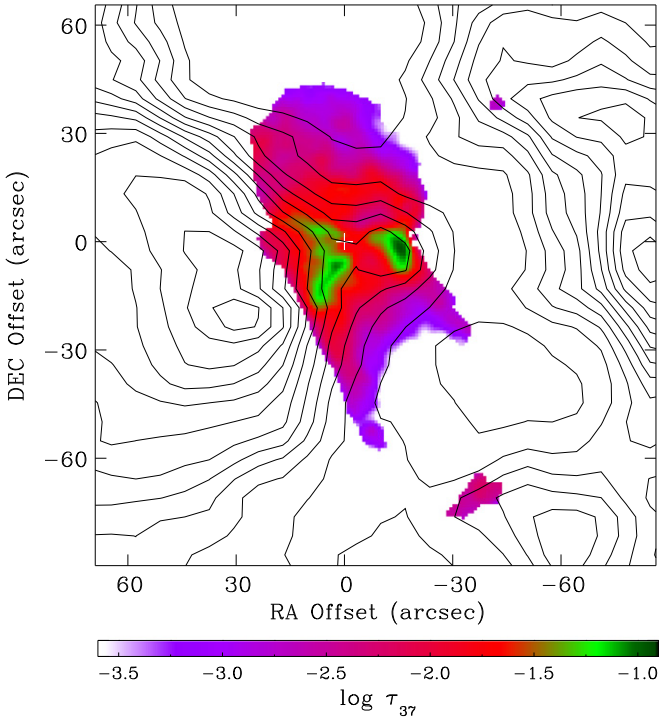

Figure 9. Optical depth τ at 37 μm along the line of sight, derived from the temperatures displayed in Figure 8. The coordinates of the map are centered near S106 IR and the coordinates are given in the caption to Figure 4. The countours represent velocity-integrated ^{13}CO (2-1) emission from IRAM observations (Schneider et al. 2002). The CO data have a spatial resolution of $\sim$11″ and the contour levels are spaced through the range 20–80 Jy/beam.

the range 8–40, with the highest extinction at position CL 1. We note that τ_{UV} does *not* necessarily increase with increasing distance from S106 IR. The amorphous silicates contribute $\sim$50%–94% to the dust mass, with the remainder contributed by amorphous carbon ($\sim$6%–50%) and, where detected, PAHs (<1%).

For WL 1–3, a mixture of PAHs, VSGs, and BGs was modeled (Figure 10). The ionized PAH model component was averaged over the IRAC instrument response for the 5.8 μm bandpass and then normalized to match the emission at 5.8 μm, which is dominated by the 6.3 μm PAH feature and contains little recombination line emission (van den Ancker et al. 2000). The IRAC 8.0 μm band contains [Ar II] and [Ar III] lines at 6.99 and 8.99 μm, respectively, and was not used to constrain the model components. Also, since the IRAC 3.6 and 4.5 μm bands conain hydrogen recombination lines, such as Pf δ (3.2970 μm), Pf γ (3.7406 μm), Br α (4.0523 μm), and Pf β (4.6539 μm; van den Ancker et al. 2000), they were not used for model fitting. Residual emission at 3.29 μm above the emission from ionized PAHs was used to normalize the neutral PAH component. We attribute excess emission at 70–350 μm to contamination from IRS 6 and emission from cooler dust along the line of sight that can be seen at both 160 μm (Figure 5) and 350 μm (Simon et al. 2012). From Table 4, values of τ_{UV} for the warm lanes are in the range 2–6. The dust mass is dominated by BGs ($\sim$91%–98%), with contributions from VSGs ($\lesssim$1%) and PAHs ($\lesssim$2%). The fraction of PAHs that are ionized spans the range 82%–97%.

SEDs and models for IRS sources, SL 1–3, and PL 1 are shown in Figure 11. We reiterate that PL 1 lies outside the MIRLIN field. The modeling approach for these sources was similar to that for WL 1–3, but the results are slightly different (Table 4). In these cases, values for τ_{UV} are in the range $\sim$0–5, with the lowest values of extinction found at the southernmost positions, SL 3 and PL 1. Again, the model composition is dominated by BGs ($\sim$50%–98%), with contributions from VSGs ($\sim$1%–43%) and PAHs ($\sim$2%–7%). The ionized PAH fractions are 88%–97%, with the higher ionization fraction values correlated with the lower values of τ_{UV}.

5. DISCUSSION

5.1. The Nature of S106 IR

5.1.1. Luminosity

The inferred effective temperature of S106 IR is consistent with a mid- to late-type O star (van den Ancker et al. 2000). However, the effective temperature of S106 IR determined by van den Ancker et al. (2000) using emission line intensities is uncertain due to opacity from the stellar/disk winds that are not included in their modeling, as well as any UV flux that is produced by accretion. Given this uncertainty, we cannot ascertain whether S106 IR is a massive binary or a single zero-age main-sequence (ZAMS) star or pre-main-sequence object. For example, the dust luminosity is higher than the luminosity of a single ZAMS star with an effective temperature of 37,000 K ($\sim$6.5 $\times$ 10^4 $L_\odot$), according to the ZAMS published in Yorke & Sonnhalter (2012) and Zinnecker & Yorke (2007). The effective temperature may be as high as 40,000 K, which would could be produced by a single ZAMS star with luminosity $\sim$1.2 $\times$ 10^5 $L_\odot$. Furthermore, S106 IR may be a pre-main sequence object on a Henyey track, resulting in a larger radius and cooler temperature than those of a ZAMS star. Thus, we cannot establish the precise nature of S106 IR in terms of binarity or evolutionary status.

5.1.2. The Circumstellar Environment

There are indications that S106 IR is a young stellar object. Its mass loss rate from winds is much higher than that of a main sequence star (Hippelein & Münch 1981; Felli et al. 1984; Drew et al. 1993; Hoare et al. 1994; Gibb & Hoare 2007; Lumsden et al. 2012). In addition, CO ν = 2–0 bandhead emission that provides evidence for a disk on AU scales (Murakawa et al. 2013). These indicators of youth allow us to place an upper limit on the age of S106 IR of $\sim$3 $\times$ 10^5 years based on the timescale for photo-evaporation of disks around massive stars (Hollenbach et al. 2000).

The variability in dust temperatures in the equatorial region is consistent with a fragmented environment that is expected from the clumpy structure of the molecular gas observed by Barsony et al. (1989) and Simon et al. (2012) and dust fragments observed by Richer et al. (1993). However, the anticorrelation between our values of τ_{UV} in the cool lanes and D_{proj} might indicate that at least some of the extinction occurs in a small (AU scale) disk that may be also be clumpy. The CO ν = 2–0 bandhead observations of Murakawa et al. (2013) imply the existence of a small disk. At the young age of S106 IR, the dispersal of the disk occurs a few AU from the star and is dominated by viscous dispersal over timescales of 10^4–10^5 years (Hollenbach et al. 2000). This suggests the possibility that the small disk may be a remnant disk or is dispersing or

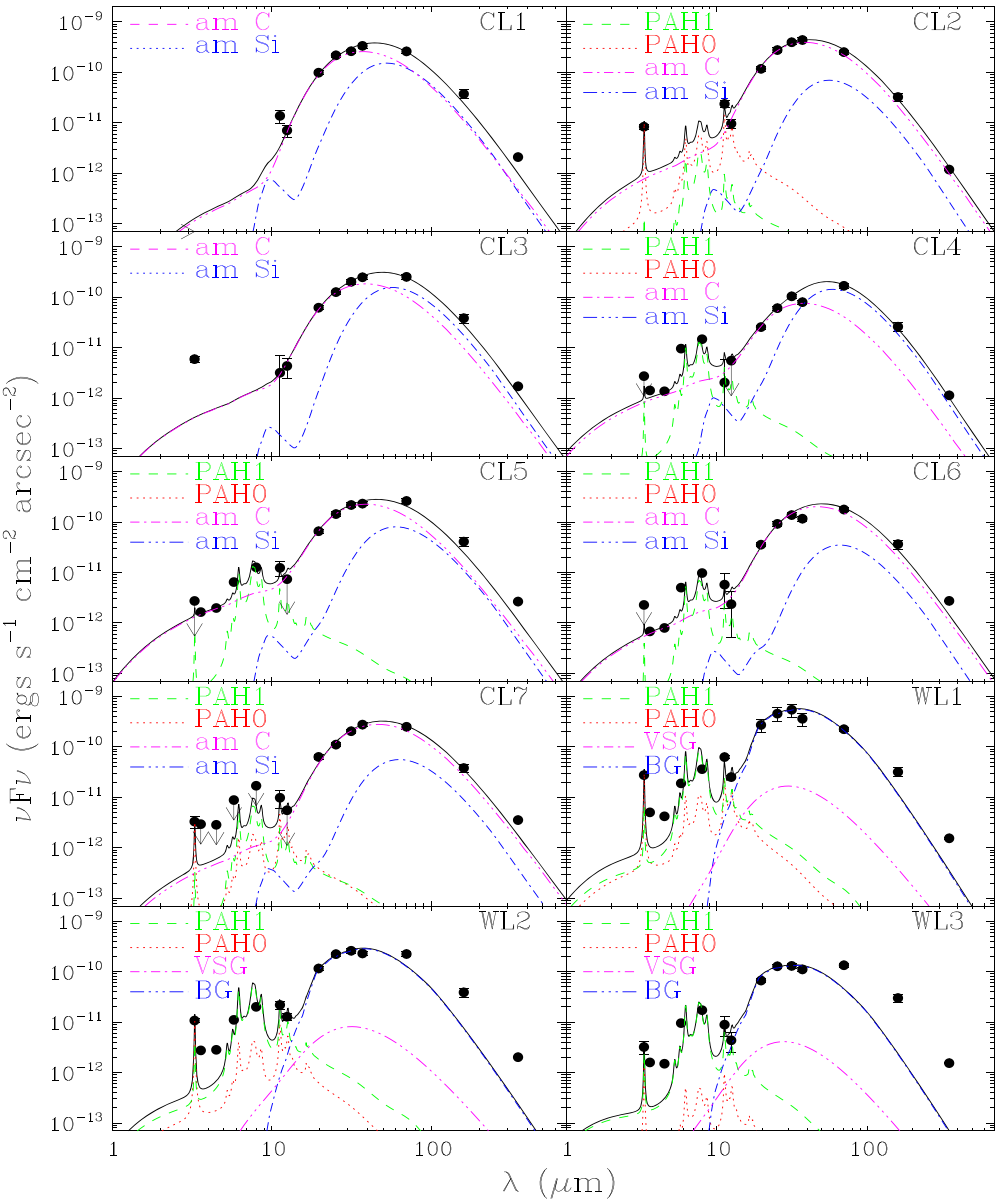

Figure 10. SEDs and model results for locations in cool lanes (CL 1–7) and warm lanes (WL 1–3). These locations are depicted in Figure 8. The total model SEDs are shown as solid black lines. For CL 1–7, the dust composition is modeled as a mixture of amorphous carbon (am C, triple-dotted–dashed magenta lines) and amorphous silicates (am Si, dotted–dashed blue lines), which in some cases contain neutral PAHs (PAH0, dotted red lines) and/or ionized PAHs (PAH1, dashed green lines). For WL 1–3, the dust grain types are changed to VSGs (triple dotted–dashed magenta lines), and BGs (dotted–dashed blue lines), and include PAHs as well. For the WL positions, the IRAC 3.6, 4.5, and 8.0 μm bands will contain emission from ionization lines (see text), and were not used to constrain the model components.

that is being supplied with gas from the surrounding bar of cold dust and gas (Peters et al. 2010).

5.2. Dust Heating

It is likely that the star illuminates dust in the lobes through an opening in the equatorial geometry of the dust. This would explain the overall lower temperatures observed near S106 IR and relatively high temperatures in the southern lobe. Smith et al. (2001) presented a color temperature map that exhibited a more uniform structure at a temperature of ∼135 K, using a λ^{-1} emissivity law. The SOFIA observations contain sensitivity that extends farther into the lobes, where the temperature gradient is more apparent, which may explain the difference in temperature gradient between the two maps.

The agreement between the observed dust color temperatures and the equilibrium temperature computed by radiative transfer in the southern lobe and PL 1, where stellar extinction is low, suggest that the dust heating is dominated by stellar radiation, rather than by grain–electron collisions or trapped Lyα heating. The following calculations support this assertion. We computed the radiative heating rate on a single grain assuming, conservatively, a moderate distance ($D = 0.15$ pc) from the star with some extinction of the UV field ($\tau_{\rm UV} = 3$), and a grain aborption efficiency $Q_\lambda = 1$ for $\lambda < 0.4\,\mu$m and $Q_\lambda \propto \lambda^{-1.6}$ for $\lambda \geqslant 0.4\,\mu$m (Draine & Lee 1984). The radiative heating rate, $\Gamma_{\rm rad}$ is given by

$$\Gamma_{\rm rad} = \frac{R_*^2}{D^2}\pi a^2 \int F_{\lambda,*} e^{-\tau_\lambda} Q_\lambda d\lambda. \quad (2)$$

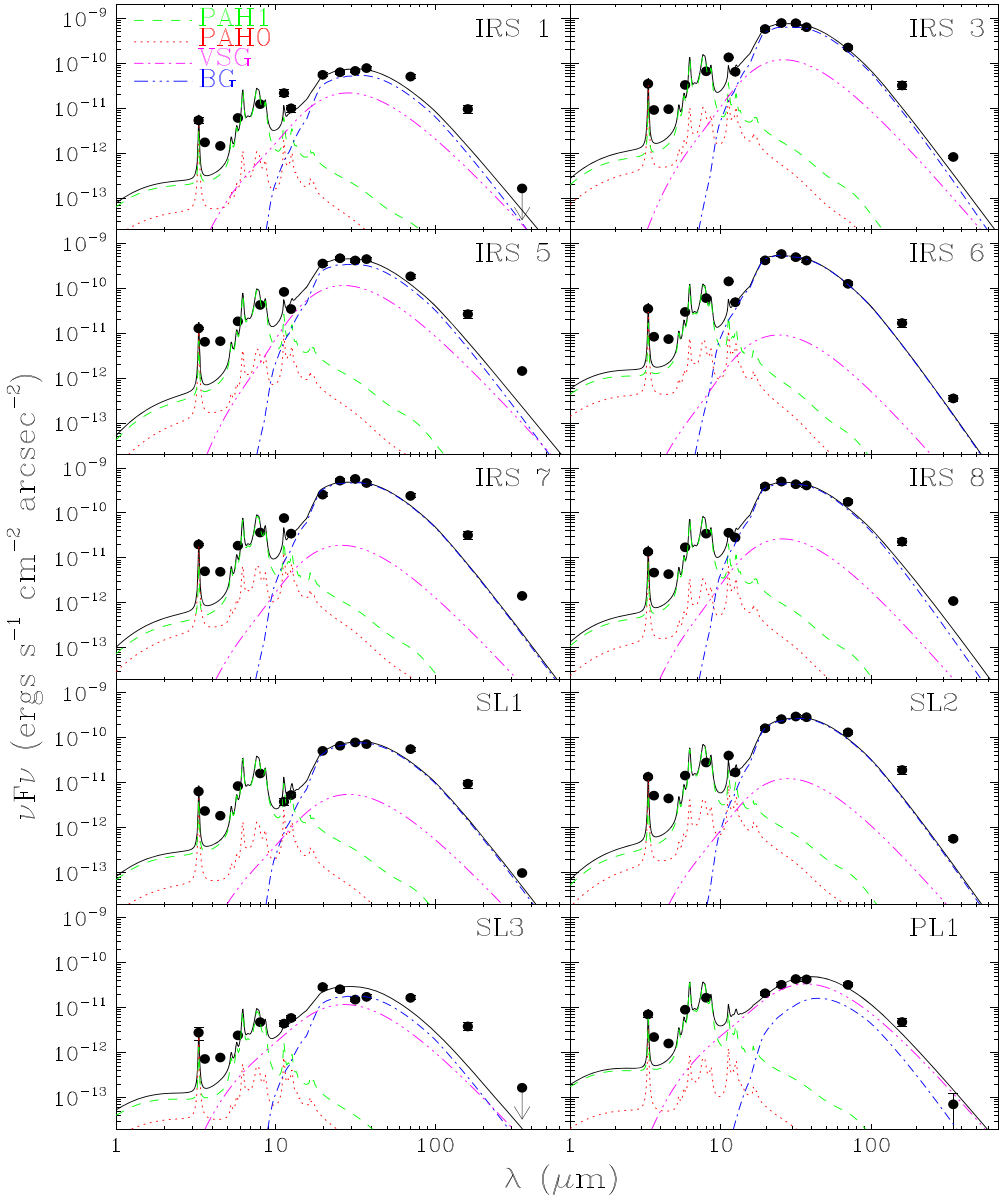

Figure 11. Same as Figure 10 for extended IRS sources (Gehrz et al. 1982), southern lobe locations SL 1–3, and southwestern clump location PL 1 (Figure 8). The model grain types for all these positions are the same as those used for the WL positions. As mentioned in the Figure 10 caption, the IRAC 3.6, 4.5, and 8.0 μm bands contains ionization lines (see text) for these positions, and were not used to constrain the model components at these positions.

Table 3
Positions, Model Parameters, and Model Results for Cool Lanes CL 1–7

Position	$D_{\rm proj}$ (pc)	$\tau_{\rm UV}$	G_0[a] (Habing)	$\alpha_{\rm C}$	$\alpha_{\rm Si}$	$f_{\rm PAH0}$	$f_{\rm PAH1}$	$f_{\rm C}$	$f_{\rm Si}$
CL 1	0.021	40	2270	−3.10	−3.50	…	…	0.300	0.700
CL 2	0.057	17	1030	−3.20	−3.50	0.002	0.001	0.488	0.509
CL 3	0.052	20	997	−3.25	−3.30	…	…	0.150	0.850
CL 4	0.14	8	463	−3.45	−3.40	…	0.001	0.062	0.936
CL 5	0.076	16	650	−3.40	−3.50	…	0.003	0.249	0.748
CL 6	0.12	13	325	−3.22	−3.50	…	0.002	0.499	0.499
CL 7	0.083	17	494	−3.10	−3.50	<0.001	0.002	0.499	0.499

Notes. $D_{\rm proj}$ is the projected distance between the specified location and S106 IR, scaled to a distance of 1.4 kpc (Schneider et al. 2007). The aperture used to derive the observed SEDs (Figure 10) for the cool lane positions was $0\farcs863 \times 0\farcs863$. Also listed are values of $\tau_{\rm UV}$, G_0 in units of the habing field, power-law size distribution indices for amorphous carbon and amorphous silicates ($\alpha_{\rm C}$ and $\alpha_{\rm Si}$, respectively) and dust mass fractions for neutral PAHs, ionized PAHs, amorphous carbon and amorphous silicates ($f_{\rm PAH0}$, $f_{\rm PAH1}$, $f_{\rm C}$ and $f_{\rm Si}$, respectively), normalized to 1.
[a] Computed using $\tau_{\rm UV}$ and $D_{\rm proj}$.

Table 4
Positions, Model Parameters, and Model Results for Warm Lane Positions WL 1–3, Extended IRS Sources from Gehrz et al. (1982), Southern Lobe Positions SL 1–3, and Southwestern Clump Position PL 1

Position	D_{proj} (pc)	τ_{UV}	G_0[a] (Habing)	α_{VSG}	α_{BG}	f_{PAH0}	f_{PAH1}	f_{VSG}	f_{BG}
WL 1	0.091	4.0	2740	−2.0	−2.9	0.003	0.014	0.004	0.979
WL 2	0.081	6.0	1850	−2.6	−2.9	0.003	0.021	0.005	0.972
WL 3	0.12	2.0	4040	−2.6	−2.9	<0.001	0.014	0.005	0.981
IRS 1	0.17	1.0	3980	−2.6	−2.9	0.002	0.027	0.061	0.910
IRS 3	0.10	2.0	5840	−2.6	−2.9	0.002	0.016	0.027	0.955
IRS 5	0.058	5.0	4700	−2.3	−2.9	0.002	0.024	0.049	0.925
IRS 6	0.14	0.3	9670	−2.6	−2.0	<0.001	0.008	0.003	0.989
IRS 7	0.079	3.0	5680	−2.6	−2.0	0.002	0.013	0.005	0.981
IRS 8	0.097	2.0	6480	−2.6	−2.9	0.001	0.013	0.009	0.977
SL 1	0.15	1.5	3620	−2.6	−2.9	0.002	0.033	0.011	0.954
SL 2	0.092	3.3	3640	−2.6	−2.9	0.002	0.021	0.007	0.970
SL 3	0.23	0.0	4380	−3.1	−2.9	0.001	0.013	0.106	0.880
PL 1	0.54	0.0	781	−2.6	−2.9	0.002	0.067	0.278	0.668

Notes. D_{proj} is the projected distance between the specified location and S106 IR, scaled to a distance of 1.4 kpc (Schneider et al. 2007). The aperture used to derive the observed SEDs (Figures 10 and 11) for these positions was $\sim 2\farcs6 \times 2\farcs6$. Also listed are values of τ_{UV}, G_0 in units of the habing field, power-law size distribution indices for VSGs and BGs (α_{VSG} and α_{BG}, respectively) and dust mass fractions for neutral PAHs, ionized PAHs, VSGs, and BGs (f_{PAH0}, f_{PAH1}, f_{VSG}, and f_{BG}, respectively), normalized to 1.
[a] Computed using τ_{UV} and D_{proj}.

The heating rate Γ_{coll} for grain–electron collisions is given by Dwek (1987):

$$\Gamma_{coll} = \left(\frac{32}{\pi m_e}\right)^{1/2} \pi a^2 n_e (kT_e)^{3/2}, \quad (3)$$

where m_e is the mass of an electron, n_e is the number density of free electrons, and T_e is the electron temperature. We assumed a typical value for the electron temperatures in a gas-cooled nebula ($T_e \approx 10{,}000$; Tielens 2005) and used an estimated value for the electron number density ($n_e \approx 3 \times 10^4\,cm^{-3}$) from Bally et al. (1983). We find the heating rate for grain–electron collisions is $\lesssim$15% that of the radiative heating. Such a small component of the heating will have little effect on the grain equilibrium temperature.

We also expect a small contribution to the dust heating from Lyα radiation due to the presence of warm gas (e.g., Schneider et al. 2002, 2003; Simon et al. 2012). The rate of this heating Γ_α is given by Tielens (2005):

$$\Gamma_\alpha = \frac{n_e^2 \beta_B h\nu_\alpha}{n_d}, \quad (4)$$

where β_B is the hydrogen recombination coefficient to all levels with $n \geqslant 2$, ν_α is the frequency of a Lyα photon, and n_d is the number density of dust particles. We assumed a high degree of ionization ($x \approx 1$), a charge neutral gas ($n_e = n_p$, where n_p is the number density of protons), and a standard gas-to-dust mass ratio of 100. For a grain with radius 0.1 μm and mass density $\rho = 3\,g\,cm^{-3}$, we find $\Gamma_\alpha \approx 3.2 \times 10^{-6}\,\Gamma_{rad}$, where Γ_{rad} is the heating rate on the grain from the star at a distance of 0.15 pc with $\tau_{UV} = 3$. Therefore, Lyα radiation will not appreciably affect the dust grain equilibrium temperatures.

5.3. Dust Composition

In the cool lane positions, the abundance ratio of amorphous carbon to amorphous silicate grains is variable, but brackets the values found in the interstellar diffuse high galactic latitude fields of Compiègne et al. (2011; 83% amorphous silicates, 17% amorphous carbon). In the regions with a stronger UV field, the relative abundances of the BGs, VSGs, and PAHs are similar to those found in the ISM (88% BGs, 6.4% VSGs, 5.9% PAHs; Désert et al. 1990) and in the M16 PDR locations (Flagey et al. 2011). The exception is the relative VSG abundance in the southern lobe location SL 3 and the southwestern clump (PL 1) is higher than at locations closer to the star. The increase in VSGs is accompanied by a relatively high proportion of ionized PAHs when compared with the other locations. The increase in relative VSG abundance is similar to that in the "reverse shell" in M16 (Flagey et al. 2011); however the "reverse shell" shows an absence of PAHs. Flagey et al. (2011) provide wind-driven grain–grain collisions as one possible explanation for the enhancement of small grains in the M16 shell. Such a process may be at work at PL 1, although another explanation may be that there is less photo-evaporation of VSGs as a consequence of the weaker radiation field at PL 1. Photo-evaporation of VSGs has been proposed to explain the abundances of VSGs and PAHs in other regions such as Ced 201 (Cesarsky et al. 2000; Berné et al. 2007), NGC 2023 north (Compiègne et al. 2008), ρ Oph-SR3 and NGC 7023-NW (Rapacioli et al. 2005), and NGC 7023-E and ρ Oph-filament (Berné et al. 2007).

5.4. Size of the Nebular Region

Hα images show that the size of the H II region extends southwest from S106 IR to an ionization front near location PL 1 (Bally et al. 1998). Theory states that the Strömgren radius of an H II region expands with time according to the equation (Ward-Thompson & Whitworth 2011):

$$R(t) \simeq 5 \left(\frac{\dot{N}_{H\,I}}{10^{50}\,s^{-1}}\right)^{1/7} \left(\frac{n_0}{10^3\ cm^{-3}}\right)^{-2/7} \left(\frac{t}{Myr}\right)^{4/7} pc, \quad (5)$$

where $\dot{N}_{H\,I}$ is the number of hydrogen-ionizing photons per second emitted by the star, n_0 is the number density of gas molecules in the surrounding molecular cloud, and t is time. If we assume $\dot{N}_{H\,I} = 4.1 \times 10^{48}\,s^{-1}$ (Sternberg et al. 2003) and

$n_0 \approx 1.4 \times 10^3$ cm^{-3} (Schneider et al. 2002), then a Strömgren radius of 0.6 pc (the distance from S106 IR to the ionization front assuming an inclination angle of 30°; Gehrz et al. 1982) is reached in $\sim 5 \times 10^4$ years. This timescale is consistent with the existence of a photo-evaporating disk, but we caution that it is only a rough estimate as n_0 may vary in the surrounding cloud.

Bipolar continuum emission extends beyond the ionization front. The size of the bipolar region depends on the accretion and outflow histories of S106 IR, and the clump at PL 1 may be a remnant, higher density clump that is still eroding from the formation of the lobes through outflow. Alternatively, it may be a clump of swept-up material at the ionization front. Either case indicates that there are complex dynamics in the bipolar region. Further study of the dynamics of the region will require multi-wavelength, spectrally resolved observations.

6. CONCLUSIONS

We have used ground-based, airborne, and space-based observations and performed radiation transfer modeling in order to study the warm dust in S106. We summarize the conclusions of this work as follows.

1. The total dust luminosity around S106 IR is $\gtrsim (9.02 \pm 1.01) \times 10^4\ L_\odot$. This luminosity is consistent with the luminosity of a mid- to late-type O star; however, due to uncertainties, we cannot establish its precise nature in terms of binarity or evolutionary status.
2. The dust temperature gradient (∼75–107 K) in the lobes is consistent with an equatorial geometry around S106 IR. The dust is heated radiatively, with little contribution from grain–electron collisions and Lyα radiation.
3. Variable dust temperatures (∼65–90 K) near the equatorial plane ($D_{\rm proj} \lesssim 0.1$ pc) indicate that the environment is fragmented ($\tau_{\rm UV} = 2$–40).
4. The dust mass composition in the H II region is composed of BGs (∼50%–98%), with the remaining contributions from VSGs (∼1%–43%) and PAHs ($\lesssim$7%). The largest proportions of both VSGs and PAHs are located in the clump PL 1.

We thank the SOFIA ground crew, flight crew, and Mission Operations for their successful execution of the SOFIA observations. We also thank an anonymous referee for making suggestions that led to the improvement of this paper. This work is based on observations made with the NASA/DLR Stratospheric Observatory for Infrared Astronomy (SOFIA). SOFIA science mission operations are conducted jointly by the Universities Space Research Association, Inc. (USRA), under NASA contract NAS2-97001, and the Deutsches SOFIA Institut (DSI) under DLR contract 50 OK 0901. Financial support for FORCAST was provided to Cornell by NASA through award 8500-98-014 issued by USRA. This work is based on observations made with the *Spitzer Space Telescope*, which is operated by JPL/Caltech under NASA contract 1407. This work is based in part on observations made with *Herschel*, a European Space Agency Cornerstone Mission with significant participation by NASA. Support for this work was provided by NASA through an award issued by JPL/Caltech. R.D.G. acknowledges support from NASA and the United States Air Force.

Facilities: *Spitzer*, SOFIA, *Herschel*.

REFERENCES

Abergel, A., Ade, P. A. R., Aghanim, N., et al. 2011, A&A, 536, A25
Adams, J. D., Herter, T. L., Gull, G. E., et al. 2012a, Proc. SPIE, 8446, 16
Adams, J. D., Herter, T. L., Osorio, M., et al. 2012b, ApJL, 749, L24
Allen, D. A., & Penston, M. V. 1975, MNRAS, 172, 245
Bally, J., & Scoville, N. Z. 1982, ApJ, 255, 497
Bally, J., Snell, R. L., & Predmore, R. 1983, ApJ, 272, 154
Bally, J., Yu, K. C., Rayner, J., & Zinnecker, H. 1998, AJ, 116, 1868
Barsony, M., Scoville, N. Z., Bally, J., & Claussen, M. J. 1989, ApJ, 343, 212
Berné, O., Joblin, C., Deville, Y., et al. 2007, A&A, 469, 575
Bieging, J. H. 1984, ApJ, 286, 591
Castelli, F., & Kurucz, R. L. 2004, arXiv:0405087
Cesarsky, D., Lequeux, J., Ryter, C., & Gérin, M. 2000, A&A, 354, L87
Compiègne, M., Abergel, A., Verstraete, L., & Habart, E. 2008, A&A, 491, 797
Compiègne, M., Flagey, N., Noriega-Crespo, A., et al. 2010, ApJ, 724, 44
Compiègne, M., Verstraete, L., Jones, A., et al. 2011, A&A, 525, 103
De Buizer, J. M., Morris, M. R., Beckline, E. E., et al. 2012, ApJL, 749, L23
Désert, F.-X., Boulanger, F., & Puget, J. L. 1990, A&A, 237, 215
Draine, B. T., & Lee, H. M. 1984, ApJ, 285, 89
Draine, B. T., & Li, A. 2007, ApJ, 657, 810
Drew, J. E., Bunn, J. C., & Hoare, M. G. 1993, MNRAS, 265, 12
Dwek, E. 1987, ApJ, 322, 812
Eiroa, C., Elsässer, H., & Lahulla, J. F. 1979, A&A, 74, 89
Fazio, G., Hora, J. L., Allen, L. E., et al. 2004, ApJS, 154, 10
Felli, M., Staude, H. J., Reddmann, T., et al. 1984, A&A, 135, 261
Flagey, N., Boulanger, F., Noriega-Crespo, A., et al. 2011, A&A, 531, A51
Gehrz, R. D., Grasdalen, G. L., Castelaz, M., et al. 1982, ApJ, 254, 550
Gibb, A. G., & Hoare, M. G. 2007, MNRAS, 380, 246
Griffin, M. J., Abergel, A., Abreu, A., et al. 2010, A&A, 518, L3
Herter, T., Helfer, H. L., Pipher, J. L., et al. 1982, ApJ, 262, 153
Herter, T. L., Adams, J. D., De Buizer, J. M., et al. 2012, ApJL, 749, L18
Herter, T. L., Vacca, W. D., Adams, J. D., et al. 2013, PASP, 125, 1393
Hippelein, H., & Münch, G. 1981, A&A, 99, 248
Hoare, M. G., Drew, J. E., Muxlow, T. B., & Davis, R. J. 1994, ApJL, 421, L51
Hodapp, K.-W., & Rayner, J. 1991, AJ, 102, 1108
Hollenbach, D. J., Yorke, H. W., & Johnstone, D. 2000, in Protostars and Planets IV, ed. I. Mannings, A. P. Boss & S. S. Russell (Tucson, AZ: Univ. Ariz. Press), 401
Hora, J. L., Bontemps, S., Megeath, S. T., et al. 2009, BAAS, 213, 356.01
Hora, J. L., Fazio, G. G., Allen, L. E., et al. 2004, Proc. SPIE, 5487, 77
Israel, F. J., & Felli, M. 1978, A&A, 63, 325
Kraemer, K. E., Hora, J. L., Adams, J. D., et al. 2010, BAAS, 215, 414.01
Landini, M., Natta, A., Oliva, E., et al. 1984, A&A, 134, 284
Lucas, A. M., Le Squeren, A. M., Kazes, I., et al. 1978, A&A, 66, 155
Lucy, L. B. 1974, AJ, 79, 745
Lumsden, S. L., Wheelwright, H. E., Hoare, M. G., et al. 2012, MNRAS, 424, 1088
Makovoz, D., & Khan, I. 2005, in ASP Conf. Ser. 132, Astronomical Data Analysis Software and Systems VI, ed. P. L. Shopbell, M. C. Britton & R. Ebert (San Francisco, CA: ASP), 81
Martins, F., Schaerer, D., & Hillier, D. J. 2005, A&A, 436, 1039
Mezger, P. G., Chini, R., Kreysa, E., & Wink, J. 1987, A&A, 182, 127
Murakawa, K., Lumsden, S. L., Oudmaijer, R. D., et al. 2013, MNRAS, 436, 511
Oasa, Y., Tamura, M., Nakajima, Y., et al. 2006, AJ, 131, 1608
Peters, T., Banerjee, R., Klessen, R. S., et al. 2010, ApJ, 711, 1017
Pipher, J. L., McMurtry, C. W., Forrest, W. J., et al. 2004, Proc. SPIE, 5487, 234
Pipher, J. L., Sharpless, S., Savedoff, M. P., et al. 1978, A&A, 59, 215
Poglitsch, A., Waelkens, C., Geis, N., et al. 2010, A&A, 518, L2
Price, S. D., Egan, M. P., Carey, S. J., et al. 2001, AJ, 121, 2819
Rapacioli, M., Joblin, C., & Boissel, P. 2005, A&A, 429, 193
Ressler, M. E., Werner, M. W., van Cleve, J., & Chou, H. A. 1994, in Infrared Astronomy with Arrays, the Next Generation, Vol. 190, ed. I. S. McLean (Berlin: Springer), 429
Richardson, W. H. 1972, JOSA, 62, 55
Richer, J. S., Padman, R., Ward-Thompson, D., et al. 1993, MNRAS, 262, 839
Roussel, H. 2013, PASP, 125, 1126
Ryter, C., Puget, J. L., & Pérault, M. 1987, A&A, 186, 312
Schaerer, D., de Koter, A., Schmutz, W., & Maeder, A. 1996, A&A, 310, 837
Schneider, N., Simon, R., Bontemps, S., et al. 2007, A&A, 474, 873
Schneider, N., Simon, R., Kramer, C., et al. 2002, A&A, 384, 225
Schneider, N., Simon, R., Kramer, C., et al. 2003, A&A, 406, 915

Schuster, M. T., MarEengo, M., & Patten, B. M. 2006, Proc. SPIE, 6270, 65
Sharpless, S. 1959, A&AS, 4, 257
Sibille, F., Bergeat, J., Lunel, M., & Kandel, R. 1975, A&A, 40, 441
Simon, R., Schneider, N., Stutzki, J., et al. 2012, A&A, 542, L12
Smith, N., Jones, T. J., Gehrz, R. D., et al. 2001, AJ, 121, 984
Stasińska, G., & Schaerer, D. 1997, A&A, 322, 615
Staude, H. J., Lenzen, R., Dyck, H. M., & Schmidt, G. D. 1982, ApJ, 255, 95
Sternberg, A., Hoffmann, T. L., & Pauldrach, A. W. A. 2003, ApJ, 599, 1333
Tielens, A. G. G. M. 2005, The Physics and Chemistry of the Interstellar Medium (Cambridge: Cambridge Univ. Press)
Tokunaga, A., & Thompson, R. 1979, ApJ, 231, 736
van den Ancker, M. E., Tielens, A. G. G. M., & Wesselius, P. R. 2000, A&A, 358, 1035
Ward-Thompson, D., & Whitworth, A. P. 2011, An Introduction to Star Formation (New York: Cambridge Univ. Press)
Werner, M. W., Roellig, T. L., Low, F. J., et al. 2004, ApJS, 154, 1
Yorke, H. W., & Sonnhalter, C. 2012, ApJ, 569, 846
Young, E. T., Becklin, E. E., De Buizer, J. M., et al. 2012, ApJL, 749, L17
Zinnecker, H., & Yorke, H. W. 2007, ARA&A, 45, 481